Droplet Fragmentation: 3D Imaging of a New Pore-scale Process during Multiphase Flow in Porous Media

Tannaz Pak[1, 2], Ian B. Butler[1, 2] ,Sebastian Geiger[2, 3], Marinus I.J. van Dijke[2, 3], Ken Sorbie[3]
1: School of Geosciences, University of Edinburgh, West Mains Road, Edinburgh EH9 3JW, UK
2: International Centre for Carbonate Reservoirs, West Mains Road, Edinburgh EH9 3JW, UK
3: Institute of Petroleum Engineering, Heriot-Watt University, Edinburgh EH14 4AS, UK

Abstract

Using X-ray computed micro-tomography (μCT), we have visualised and quantified the in-situ structure of a trapped non-wetting phase (oil) in a highly heterogeneous carbonate rock after injecting a wetting phase (brine) at low and high capillary numbers. We imaged the process of capillary desaturation in 3D and demonstrated its impacts on the trapped non-wetting phase cluster size distribution. We have also identified a new pore-scale event during capillary desaturation. This pore-scale event, described as droplet fragmentation of the non-wetting phase, occurs in larger pores. It increases volumetric production of the non-wetting phase after capillary trapping and enlarges the fluid-fluid interface, which can enhance mass transfer between the phases. Droplet fragmentation therefore has implications for a range of multi-phase flow processes in natural and engineered porous media with complex heterogeneous pore spaces.

Significance Statement

Fluid displacement processes in carbonate rocks are important because they host over 50% of the world's hydrocarbon reserves and are aquifers supplying water to one quarter of the global population. A new pore-scale fluid displacement event, droplet fragmentation, is described which occurs during the flow of two immiscible fluids specifically in carbonate rocks. The complex, heterogeneous pore structure of carbonate rocks induces this droplet fragmentation process which explains the increased recovery of the non-wetting phase from porous carbonates as the wetting phase injection rate is increased. The new displacement mechanism has implications for i) enhanced oil recovery, ii) remediation of non-aqueous liquid contaminants in aquifers and iii) subsurface CO_2 storage.

Introduction

Multi-phase fluid displacement processes in porous media are important for a broad range of natural and engineering applications such as transport of non-aqueous phase liquid contaminants in aquifers, oil and gas production from hydrocarbon reservoirs, subsurface CO_2 storage, or gas transport in fuel cells. Herein, capillary trapping is a fundamental mechanism that causes immobilisation of a portion of the resident non-wetting phase when it is displaced by an invading wetting phase. As a result, production of the non-wetting phase is always less than 100%.

The pore-scale physics of capillary trapping are broadly understood as the underlying mechanisms such as piston-like displacement, snap-off and film development have been observed in physical micro-model experiments and quantitative theories have been established for them (1-4). During drainage (i.e. where a non-wetting phase displaces the wetting phase), the wetting phase can establish films in the corners of the pores which results in its continuous production and hence low residual saturations of the wetting phase. During imbibition (i.e. where the wetting phase displaces a non-wetting phase), swelling of the wetting films causes snap-off of the non-wetting phase, which results in capillary trapping of the non-wetting phase. The trapped non-wetting phase exists as disconnected ganglia within the pore network. Numerical pore network models have been developed and include these pore-level mechanisms with the aim of predicting the macroscopic flow properties of porous materials such as the structure of the phase distributions, residual saturation, relative permeability functions, and capillary pressure curves (5-8).

The saturation distribution of two immiscible fluid phases in a porous medium is influenced by the wettability of the system, i.e. the distribution of surfaces that are preferentially water wet or preferentially wetting to a non-aqueous phase such as oil (9). It is well-known that a trapped non-wetting phase can be re-mobilized and recovered when the wetting phase is injected at capillary numbers N_c that exceed a critical level. N_c is a dimensionless ratio quantifying the relative importance of viscous to capillary forces, i.e. $N_c = q\mu/\sigma$ where q is the flow rate, μ the viscosity of the invading phase and σ the interfacial tension (10). For homogeneous sandstones remobilisation typically occurs at N_c of the order of 10^{-5}, an effect known as capillary desaturation (11).

Recent advances in X-ray computed micro-tomography (μCT) methods have enabled the visualisation and quantitative analysis of the static distribution of fluid phases, fluid rock interactions and the structure of wetting and non-wetting phases in porous materials (8, 12). A particular focus has been on capillary trapping (13-17). Using synchrotron X-ray μCT facilities, it has also become possible to visualise dynamic pore-scale mechanisms, including snap-off and Haines jumps (18). Most of these imaging studies have focused on relatively homogeneous pore systems such as bead packs (19), sand packs (19-23), and sandstones (8, 15, 18, 20), but less attention has been paid to carbonate rocks. However, more than 50% of the world's remaining oil reserves are located in carbonate reservoirs (24) and carbonate aquifers supply water wholly or partially to one quarter of the global population (25). Carbonates rocks can have complex multi-scale pore structures, which render the application of X-ray μCT more challenging because of the need to select a representative sample which is small enough to achieve high resolutions on μCT images but which also captures the essential heterogeneities of the pore-structure (26, 27).

In this contribution we use X-ray μCT to quantify the structure and distribution of a non-wetting phase (oil) after drainage and after its displacement by a wetting phase (brine) at low and high capillary numbers in a heterogeneous carbonate with multiple pore-scales. Using image analysis, we demonstrate the effect of capillary desaturation on the cluster size distribution of the trapped oil phase. We also identify a new pore-scale event, which we refer to as droplet fragmentation. Droplet fragmentation is responsible for further production of the oil phase beyond capillary trapping. This fragmentation process occurs mainly in larger pores. It results in the production of additional oil from these large pores, contributes to a change in the structure of residual oil, and increases the oil-brine surface area. As a consequence, the trapped phase may subsequently be more difficult to mobilise after droplet fragmentation has occurred but mass transfer between the phases can increase.

Cluster Size Distribution

We have analysed the size distributions of oil clusters after (a) injection of a mineral oil into a brine wetted and saturated heterogeneous carbonate core (drainage), and (b) subsequent brine injection (imbibition). Initially, the carbonate was fully saturated with brine. During drainage, the oil saturation was established using first a slow oil injection at a rate of q = 10 μl min^{-1} ($N_c = 7.2\times10^{-7}$) followed by a fast oil injection at a rate of q = 700 μl min^{-1} ($N_c = 4.9\times10^{-5}$). Brine was subsequently injected at the same flow rates ($N_c = 2.02\times10^{-7}$, $N_c = 1.54\times10^{-5}$), respectively. At each stage 10 pore volumes of the displacing fluid were injected. After each injection step, the flow cell was scanned using μCT under static (i.e. no flow) conditions (Table SI1).

The digital volumes obtained by μCT were segmented into three binary volumes, each representing the discrete oil, brine, or rock component. The binary images of the two fluid phases were

subsequently labelled such that any group of connected voxels were assigned an individual label, thus constituting a fluid cluster. Only the central 18 mm of the 44 mm long carbonate core was used for quantitative analysis presented here to avoid artefacts from capillary end effects. Fig. 1 shows 3D renderings of the oil phase after drainage and imbibition at the two different flow rates. The oil saturations in the central section of the sample were 0.86 and 0.69 after drainage (at q = 10µl min^{-1} and q = 700 µl min^{-1}, respectively) and 0.54 and 0.44 after imbibition (at q = 10µl min^{-1} and q = 700µl min^{-1}, respectively). Two independent scans separated by 22 hours show that the fluid saturations exhibited a considerable degree of redistribution after the 700 µl min^{-1} oil injection was ceased. Fig. 1B shows the image acquired after the fluid redistribution. This auto-redistribution was caused only by the capillary forces acting at the pore level since the density of the two phases was closely matched. Fig. 1B shows the oil clusters imaged after the redistribution.

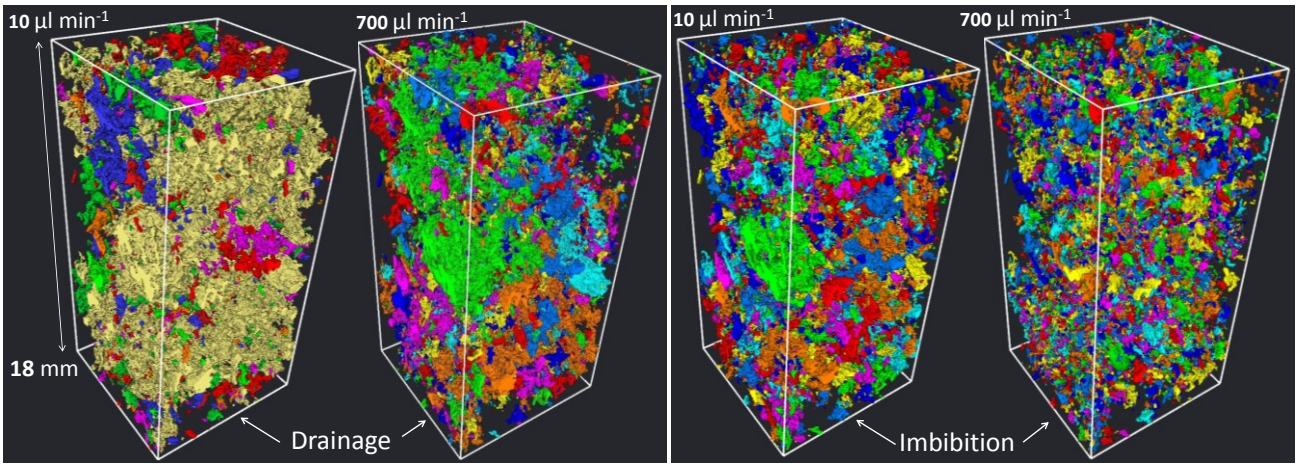

Figure 1: 3D rendering of the oil clusters after drainage and imbibition at high and low flow rates. Discrete clusters were rendered in different colours. Large clusters existed after drainage were broken down to numerous smaller clusters after imbibition.

Fig. 2 shows the oil cluster size distribution after each individual injection step during drainage and imbibition. In this context, droplet refers to oil blobs smaller than the pores confining them, while cluster is a more general term describing oil ganglia saturating a number of neighbouring pores, single pores, or a fraction of pores. Fig. 2A shows the distribution of the normalised oil volume in clusters of a certain size as a function of the cluster volumes (logarithmic, e.g. for the first bin 10 < oil cluster volume < 100). Cluster volumes range from 10 voxels for the smallest clusters to 10^7 for the largest clusters. Clusters smaller than 10 voxels were excluded to eliminate the influence of noise in the raw data. During both drainage processes large, and probably sample-spanning, clusters existed with volumes exceeding 10^7 voxels (Figs. 1A and 1B). Fig. 2B shows the cluster frequency as a function of the same cluster volumes for each bin for the drainage and imbibition steps. This analysis leads to four key observations: (i) The largest oil cluster after drainage at 10 µl min^{-1} contained 76 % of the total oil volume. This cluster, rendered in yellow in Fig. 1A, is clearly a percolating cluster, i.e. it connects to the inlet and outlet of the analysed volume. At this stage the total number of clusters was 4142. (ii) Drainage at 700 µl min^{-1} and the subsequent fluid redistribution caused the oil saturation to reduce by 17% as a result of oil migration out of the central region of core plug. The total number of oil clusters almost doubled (i.e. increased to 7561). (iii) After imbibition at 10 µl min^{-1}, the saturation of oil further reduced by 15%. The total number of oil clusters increased to 9054. The volumetric

cluster size distribution shows a peak between 10^5 and 10^6 voxels, which is two orders of magnitude smaller than the peak recorded for both drainage processes. Clusters larger than 10^7 voxels and spanning the analysed volume were absent. (iv) After imbibition at 700 µl min^{-1}, the oil saturation decreased by a further 10%. Further break-down of the oil clusters occurred, doubling the total number of oil clusters present to 18130. The continuous increase in cluster number and decrease in cluster size during both imbibition steps suggests that the oil clusters were trapped. However, additional oil was mobilised when brine injection rate was increased.

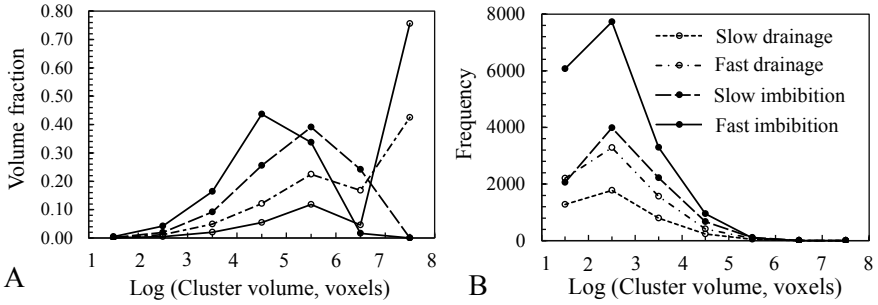

Figure 2: Volume based (A) and number based (B) cluster size distribution after the four injection steps shown in Fig. 1. Note the large oil clusters with volumes above 10^7 voxels existed after the drainage steps. A continuous increase in number of clusters along with decrease in the cluster volumes indicates the change in oil structure during the drainage and imbibition processes.

Dominant Pore-scale Fluid Displacement Mechanisms

Fig. 3 A-D show example µCT slices after each injection step. They indicate that the plug is preferentially water wet as the brine-oil contact angles (measured through brine) are below 90° (Figs. 3C and 3D). Brine films in the corners of the pores after drainage cannot be resolved due to partial volume effects caused by the difference in X-ray attenuation of the two fluid phases. However, the apparent increase in the brine films' thickness during imbibition (Fig. 3C) suggests that brine films were present.

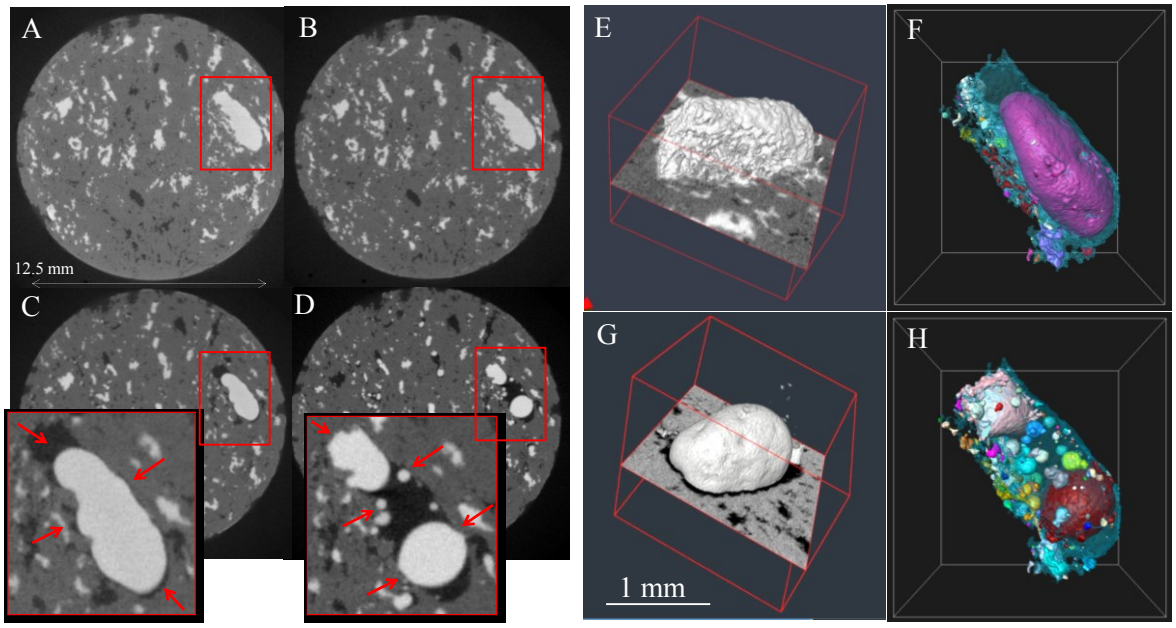

Figure 3: (A-D) Example µCT slices after the four injection steps shown in Fig.1. (E, G) 3D rendering of oil phase in the area highlighted in B and C, respectively. (F, H) 3D rendering of the labelled oil phase respectively at (C from another view, D). The discrete oil droplets are rendered in different colours while the blue transparent surface shows the brine phase. The large isolated oil droplet shown in C, F, and G is trapped because of a snap-off event and cannot be produced from the pore in this capillary dominated regime (N_c=2.02 × 10^{-7}). Red arrows indicate a visible brine film surrounding the isolated droplet of oil after snap-off (C) and fragmented droplets after fast imbibition (D).

Figs. 3E and 3F show 3D renderings of the oil phase and demonstrate how the oil phase in the largest pore in Figs. 3B and 3C evolved during imbibition at 10 µl min^{-1}. Prior to this slow imbibition process, the oil phase in this large pore was part of a well-connected cluster spanning multiple individual neighbouring pores and throats (Fig. 3E). Following slow imbibition the narrow throats in the neighbourhood of the large pore were filled with brine such that the large oil cluster was broken up into 83 oil droplets trapped in the large pore and its neighbours. This observation is consistent with snap-off of oil by brine films swelling in the pore throats. The large isolated oil droplet shown in Figs. 3C, 3F and 3G was trapped by the snap-off events, as it could not be displaced in this capillary dominated flow regime. 3D renderings of the labelled oil phase remaining after fast imbibition at 700 µl min^{-1} (Fig. 3H) show the presence of 276 oil droplets trapped in the same large pore (and in its neighbours) as shown in Fig. 3F. Of these droplets, 89% had volumes that were smaller than the volume of the original, i.e. largest, oil droplet before fast imbibition by at least two orders of magnitude (see Fig. SI8). All oil droplets were in contact with the rock surface. The fragmentation of a large trapped oil droplet into many smaller droplets at high capillary numbers was observed throughout the core (see Figs. SI4 and SI5).The fragmentation of oil into multiple discrete droplets was most strikingly observed in the larger pores, but it also occurred in pores with volumes spanning over three orders of magnitudes, from 10^8 to 10^{10}µm^3 (Figs. SI4 and SI5). Note that the observation and quantitative analysis of this effect within pores with volumes smaller than 10^8 µm^3 was limited by image resolution.

The work done by the viscous forces that are exerted on trapped oil clusters in the pore space of the core during high flow rate imbibition caused the clusters to break up into droplets, which increased the total surface area of the oil-brine interface and hence the interfacial energy.

Analysis of Fragmented Oil Droplets

Fragmentation Energy: A suspended oil droplet forms a spherical shape to minimize its surface area (A) and so surface free energy ($\sigma_{ob}A$). Most fragmented droplets have shapes that are close to spherical (Fig. SI8 provides a measure of the sphericity of the fragmented oil droplets). We assume an oil-brine (σ_{ob}) and oil-solid (σ_{os}) interfacial tension of 35mNm^{-1} and 5mNm^{-1} (28), respectively, and estimate the change in surface energy ΔE during fragmentation displacement as

$$\Delta E = \frac{A_o\sigma_{ob} - NA_i[(1-f)\sigma_{ob} + f\sigma_{os}]}{A_o\sigma_{ob}}, \quad (1)$$

that is the increase in interfacial energy due to fragmentation into N droplets divided by the surface energy of the original droplet. Note that a fraction f of the fragmented oil droplets' surface area is assumed to be in contact with the rock surface. The low oil-solid interfacial tension in this fraction stabilises the fragmented droplets. For any given droplet of arbitrary size a minor change in incremental energy (i.e. less than five times the original droplet's surface energy) is required to extensively fragment the droplet. For instance, a droplet with radius of 50 μm requires ΔE approximately 5.3×10^{-9} J to be fragmented into 200 smaller droplets. This is the maximum energy required considering $f = 0$. The required ΔE decreases as f increases. Fig. 4 shows the additional relative energy required to fragment an oil droplet of arbitrary size into N smaller oil droplets. These calculations indicate that droplet fragmentation can occur for relatively small changes in interfacial energy.

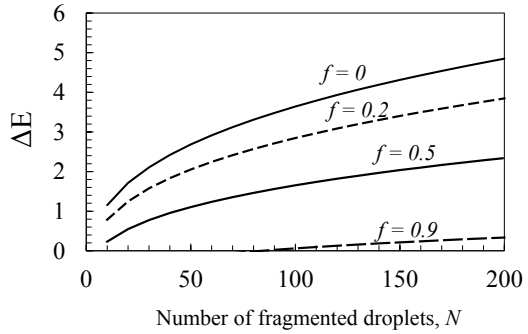

Figure 4: Additional energy for fragmentation of an oil droplet of arbitrary size relative to the surface energy of the original oil droplet as a function of the number of fragments N and the fraction of the droplet's surface that is in contact with the rock, f. The additional energy required for fragmentation is less than five times the original surface energy, which indicates that droplet fragmentation can occur for relatively small changes in interfacial energy that are consistent with the fluid properties used in the experiments.

Statistical Analysis of the Remaining Fragmented Droplets: The overall increase in oil recovery due to fragmentation events is 10% of the initial oil saturation. The three pores depicted in Fig. 3 and Figs. SI4 and SI5 have volumes of 10^{10}, 10^9, and 10^8 μm^3, respectively. The volume fraction of the recovered oil as a result of fragmentation displacement is 68%, 38 %, and 52%, respectively, of the oil trapped in these three pores after the slow imbibition. This change constitutes significant oil production that was initiated by fragmentation displacement and may explain published experimental observations of capillary desaturation at increasing capillary numbers (11) and in particular in rocks such as carbonates which comprise a wide pore size distribution.

Stability of the Fragmented Oil Droplets: The fragmented droplets were static in the same configuration in scans separated by over 24 hours and did not move during the three hour period of data acquisition for each scan. All fragmented oil droplets were in contact with the pore surface and

stabilised by their contact with the mineral surface, relative to droplets freely dispersed in suspension (Fig. SI3). This condition of dispersed droplets attached to the mineral wall of the pore is metastable with respect to an un-fragmented oil droplet, as discussed above.

For the pore shown in Fig.3 droplet fragmentation increased the oil-brine interfacial area as well as the oil-rock contact surface per unit volume of oil by factors of 1.62 and 4.12, respectively. The *f* values (per unit volume of oil) therefore increased from 0.24 to 0.43, providing more stabilisation for the fragmented oil droplets. For interfacial area calculations we refer to (23). The change in interfacial energy ΔE of the oil phase was 0.73 of the initial energy of the trapped oil before fragmentation (6.4×10^{-7} J). The fragmentation energy calculations for pores with volumes 10^{10} and 10^{8} μm^3 are presented in Table SI2, and Fig.SI6.

Cluster size Analysis – Percolation Theory:

Percolation theory suggests that size distribution of the trapped non-wetting phase clusters in a porous media after imbibition at infinitesimally low flow rates should scale as a power-law $N(s) \sim s^{-\tau}$ (29, 30) where s is the number of pores saturated by a trapped non-wetting cluster and τ is the power-law exponent. For 3D structures, numerical simulations suggest that τ is typically larger than 2 (30-33). Values of τ larger than 2 were also observed in direct measurements of trapped cluster distributions in clastic rocks and synthetic porous media (13, 16, 17).

Fundamentally, percolation theory can only be applied to capillary-dominated flow with infinitesimally slow displacement rates. Therefore, here we only discuss the data obtained after the slow imbibition. It is possible to fit portions of the trapped oil "volume" distribution with a number of power-law functions such that $\tau \geq 2$. However, the entire range of the data does not fit a single power-law function (Fig. 5). According to percolation theory, a power-law behaviour is only applicable if the cluster size is defined as the number of pores occupied and not the volume of the clusters (34). In homogeneous pore structures with narrow pore size distributions, the pore number-to-volume scaling approaches 1:1. Hence, the cluster sizes measured in volume using X-ray μCT imaging can closely replicate the number of pores occupied by the clusters. However, for heterogeneous pore systems with a wide pore size distribution, the pore number-to-volume scaling is no longer 1:1, therefore the number of pores occupied by clusters cannot be deduced from the volume of clusters. Further, the power-law scaling is valid only for clusters with $s > 1$ (34) (i.e. the by passed oil clusters and not the clusters trapped in single pores as a result of snap-off). The power-law applies to distributions excluding the clusters that only occupy a single pore (17).

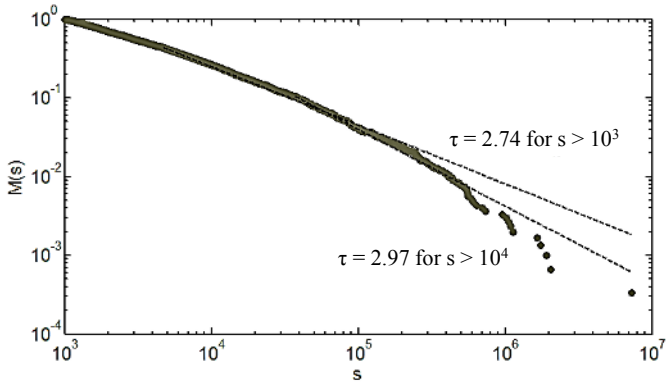

Figure 5: Cumulative cluster size probability distribution M(s) as a function of cluster size s, measured in voxels, calculated using a maximum likelihood estimator (35). It is possible to fit portions of the trapped oil "volume" distribution with a number of power-law functions such that $\tau \geq 2$. However, the entire range of the data does not fit a single power-law function.

Summary and Conclusions

Using X-ray μCT imaging and quantitative analysis of fluid phase distributions during drainage and imbibition processes (at low and high capillary numbers) in a heterogeneous carbonate core, we were able to visualise and identify features consistent with known pore-scale displacement mechanisms such as piston like and snap-off events. In addition, we present evidence for a new pore-scale mechanism that we term droplet fragmentation, which occurs at high capillary numbers. The experimental data suggests that droplet fragmentation significantly contributes to capillary desaturation at high capillary numbers in porous media with heterogeneous and multi-scale pore systems.

Droplet fragmentation of the trapped oil phase was observed in the larger pores of the carbonate, spanning at least three orders of magnitude in volume ranging between 10^8 - 10^{10} μm^3. The increase of viscous forces in these larger pores at higher capillary number is consistent with a small change in interfacial energy, which could cause larger trapped oil droplets to fragment into numerous smaller ones. These fragmented droplets are close to spherical shape to minimise their surface free energy.

Droplet fragmentation has a range of implications for understanding, quantifying and modelling of multi-phase fluid flow processes in a number of applications including the remediation of non-aqueous phase liquid contaminants in groundwater aquifers, subsurface CO_2 storage, and enhanced oil recovery. Droplet fragmentation changes the structure of the residual non-wetting phase, and hence increases the recovery of the non-wetting phase. Droplet fragmentation also enlarges the surface area between the wetting and non-wetting phase. The increase in surface area enhances mass transfer between both phases, which can be important for all these applications.

For example, in groundwater remediation, fragmentation displacement could not only lower the residual saturation of the trapped non-aqueous phase and mobilise this phase, it also increases the fluid-fluid surface area which improves the effectiveness of surfactant addition and can accelerate the rate at which inorganic reagents and/or microbial treatments degrade non-aqueous phase liquids, (36, 37). Similarly, during enhanced oil recovery, droplet fragmentation could reduce the residual oil saturation and enhance the rate at which chemicals and gases dissolve in oil (38). Both effects may increase oil recovery but issues of re-coalescence and mobilisation remain.

The dissolution of trapped CO_2 in brine during solubility trapping is an important mechanism for secure subsurface CO_2 sequestration (39, 40). An increased CO_2-brine surface area due to droplet fragmentation can accelerate this process. Although droplet fragmentation may be limited to carbonate formations as they normally contain a wide range of pore-sizes, it is expected that this mechanism is still of global importance considering that about 50% of the world's hydrocarbon reserves and a major host to the world's groundwater resources. Droplet Fragmentation is an additional mechanism that may need to be included in pore-scale models of displacement processes.

Materials and Methods

Two-phase core flooding experiments were performed integrating μCT and a custom built X-ray transparent core holder (operating pressure to 690 kPa) to directly visualise fluid saturation distributions in a carbonate pore structure at pore-scale. The carbonate sample is an outcrop Silurian dolomite (Thornton Formation, USA) with a diameter of 12.5mm and length of 44 mm ($\varphi \sim 17$ %, $K \sim 50$ md). The non-wetting phase is a mineral oil (50% 1-iododecane and 50% dodecane), the wetting phase is a 0.03 Molar aqueous solution of KI. This provided an excellent contrast between the two fluid phases and the rock on the acquired μCT images as well as an exact match between the densities of the two fluid phases (1.005 gr/cm^3) which eliminated the potential for gravity driven fluid redistribution during data acquisition. Image reconstructions were made using Octopus (8.5) (41) and post-processing and quantifications were performed using Avizo Fire Versions 6.0 to 8.0. All tomographic data are at 11.25 μm per voxel resolution.

Acknowledgements:

We would like to thank Petrobras and BG Group for their financial support and the permission to publish this work. We also thank Rodrigo Surmas for providing rock samples, Petrobras Research Centre (CENPES) for the mercury injection capillary pressure tests, Robert Brown and Alex Hart for manufacturing the core flooding cell, Mike Hall for preparing thin sections of our rock samples, and the Centre of Environmental Scanning Microscopy at Heriot-Watt University for SEM images.

References:

1. Lenormand R, Zarcone C, & Sarr A (1983) Mechanisms of the displacement of one fluid by another in a network of capillary ducts. *Journal of Fluid Mechanics* 135:337-353.
2. Vizika O, Avraam DG, & Payatakes AC (1994) On the Role of the Viscosity Ratio during Low-Capillary-Number Forced Imbibition in Porous Media. *Journal of Colloid and Interface Science* 165(2):386-401.
3. Avraam DG & Payatakes AC (1995) Flow regimes and relative permeabilities during steady-state two-phase flow in porous media. *Journal of Fluid Mechanics* 293:207-236.
4. Ryazanov AV, van Dijke MIJ, & Sorbie KS (2009) Two-Phase Pore-Network Modelling: Existence of Oil Layers During Water Invasion. *Transp Porous Med* 80(1):79-99.
5. Blunt MJ (2001) Flow in porous media — pore-network models and multiphase flow. *Current Opinion in Colloid & Interface Science* 6(3):197-207.
6. Meakin P & Tartakovsky AM (2009) Modeling and simulation of pore-scale multiphase fluid flow and reactive transport in fractured and porous media. *Reviews of Geophysics* 47(3):RG3002.
7. Blunt MJ, Jackson MD, Piri M, & Valvatne PH (2002) Detailed physics, predictive capabilities and macroscopic consequences for pore-network models of multiphase flow. *Advances in Water Resources* 25:1069-1089.
8. Blunt MJ*, et al.* (2013) Pore-scale imaging and modelling. *Advances in Water Resources* 51(0):197-216.

9. Anderson W (1986) Wettability literature survey-part 2: Wettability measurement. *Journal of Petroleum Technology* 38(11):1,246-241,262.
10. Bear J (1988) *Dynamics of Fluids in Porous Media* (Dover Publication).
11. Morrow NR, Chatzis I, Thuraisingham ST, Kuntamukkula M, & Lim HT (1982) Measurement and correlation of conditions for entrapment and mobilization of residual oil. First annual report. p Medium: X; Size: Pages: 63.
12. Wildenschild D & Sheppard AP (2013) X-ray imaging and analysis techniques for quantifying pore-scale structure and processes in subsurface porous medium systems. *Advances in Water Resources* 51(0):217-246.
13. Iglauer S, Paluszny A, Pentland CH, & Blunt MJ (2011) Residual CO2 imaged with X-ray micro-tomography. *Geophysical Research Letters* 38(21):L21403.
14. Armstrong RT, Porter ML, & Wildenschild D (2012) Linking pore-scale interfacial curvature to column-scale capillary pressure. *Advances in Water Resources* 46(0):55-62.
15. Herring AL*, et al.* (2013) Effect of fluid topology on residual nonwetting phase trapping: Implications for geologic CO2 sequestration. *Advances in Water Resources* 62, Part A(0):47-58.
16. Andrew M, Bijeljic B, & Blunt MJ (2013) Pore-scale imaging of geological carbon dioxide storage under in situ conditions. *Geophysical Research Letters* 40(15):3915-3918.
17. Andrew M, Bijeljic B, & Blunt MJ (2014) Pore-scale imaging of trapped supercritical carbon dioxide in sandstones and carbonates. *International Journal of Greenhouse Gas Control* 22(0):1-14.
18. Berg S*, et al.* (2013) Real-time 3D imaging of Haines jumps in porous media flow. *Proceedings of the National Academy of Sciences of the United States of America* 110(10):3755-3759.
19. Al-Raoush RI & Willson CS (2005) A pore-scale investigation of a multiphase porous media system. *Journal of Contaminant Hydrology* 77(1–2):67-89.
20. Turner ML*, et al.* (2004) Three-dimensional imaging of multiphase flow in porous media. *Physica A: Statistical Mechanics and its Applications* 339(1–2):166-172.
21. Wildenschild D*, et al.* (2005) Quantitative analysis of flow processes in a sand using synchrotron-based X-ray microtomography. *Vadose Zone Journal* 4(1):112-126.
22. Culligan KA, Wildenschild D, Christensen BSB, Gray WG, & Rivers ML (2006) Pore-scale characteristics of multiphase flow in porous media: A comparison of air–water and oil–water experiments. *Advances in Water Resources* 29(2):227-238.
23. Porter M & Wildenschild D (2010) Image analysis algorithms for estimating porous media multiphase flow variables from computed microtomography data: a validation study. *Comput Geosci* 14(1):15-30.
24. Burchette TP (2012) Carbonate rocks and petroleum reservoirs: a geological perspective from the industry. *Geological Society, London, Special Publications* 370:17-37.
25. Hartmann A, Goldscheider N, Wagener T, Lange J, & Weiler M (2014) Karst water resources in a changing world: Review of hydrological modeling approaches. *Reviews of Geophysics*:2013RG000443.
26. Remeysen K & Swennen R (2008) Application of microfocus computed tomography in carbonate reservoir characterization: Possibilities and limitations. *Marine and Petroleum Geology* 25(6):486-499.
27. V. Hebert CG, L. Luquot, P. A. Pezard and P. Gouze (2014) Multi-scale X-ray tomography analysis of carbonate porosity. *The Geological Society of London* v. 406, doi:10.1144/SP406.12.
28. Gassin P-M, Martin-Gassin G, Meyer D, Dufrêche J-F, & Diat O (2012) Kinetics of Triton-X100 Transfer Across the Water/Dodecane Interface: Analysis of the Interfacial Tension Variation. *The Journal of Physical Chemistry C* 116(24):13152-13160.
29. Stauffer D (1981) Scaling properties of percolation clusters. *Disordered Systems and Localization,* Lecture Notes in Physics, eds Castellani C, Di Castro C, & Peliti L (Springer Berlin Heidelberg), Vol 149, pp 9-25.
30. Lorenz CD & Ziff RM (1998) Precise determination of the bond percolation thresholds and finite-size scaling corrections for the sc, fcc, and bcc lattices. *Physical Review E* 57(1):230-236.
31. D Wilkinson JFW (1980) Invasion percolation: a new form of percolation theory. *J. Phys. A: Math. Gen.* 13(5):L147.
32. Strenski PN, Bradley RM, & Debierre J-M (1991) Scaling behavior of percolation surfaces in three dimensions. *Physical Review Letters* 66(10):1330-1333.
33. Blunt MJ & Scher H (1995) Pore-level modeling of wetting. *Physical Review E* 52(6):6387-6403.
34. Wilkinson D (1986) Percolation effects in immiscible displacement. *Physical Review A* 34(2):1380-1391.

35. Clauset A, Shalizi CR, & Newman ME (2009) Power-law distributions in empirical data. *SIAM review* 51(4):661-703.
36. Imhoff PT & Miller CT (1996) Dissolution Fingering During the Solubilization of Nonaqueous Phase Liquids in Saturated Porous Media: 1. Model Predictions. *Water Resources Research* 32(7):1919-1928.
37. McCray JE, Bai G, Maier RM, & Brusseau ML (2001) Biosurfactant-enhanced solubilization of NAPL mixtures. *Journal of Contaminant Hydrology* 48(1–2):45-68.
38. Lake LW (1989) *Enhanced Oil Recovery* (Prentice Hall).
39. Riaz A, Hesse M, Tchelepi HA, & Orr FM (2006) Onset of convection in a gravitationally unstable diffusive boundary layer in porous media. *Journal of Fluid Mechanics* 548:87-111.
40. Neufeld JA*, et al.* (2010) Convective dissolution of carbon dioxide in saline aquifers. *Geophysical Research Letters* 37(22):L22404.
41. Vlassenbroeck J*, et al.* (2010) Octopus 8: A High Performance Tomographic Reconstruction Package for X-ray Tube and Synchrotron micro-CT. *Advances in X-ray Tomography for Geomaterials*, (ISTE), pp 167-173.

Supporting Information

Experimental Materials and Conditions

Table SI1 lists the test cycle used in the experiments. Injections used two constant flow rates of 10 and 700 µl min^{-1}, which were chosen such that flow was dominated by capillary and viscous forces, respectively, at different stages during drainage and imbibition.

Table SI1: Fluid injections and X-ray µCT scanning steps during slow and fast drainage and imbibition.

Injection step	Flow Rate ($\mu l\ min^{-1}$)	Capillary Number	Linear Velocity ($\mu m s^{-1}$)	Injection Period (hrs)	Pore Volumes Injected
Slow oil injection	10	7.2×10^{-7}	7.68	18	10
Forced oil injection	700	4.9×10^{-5}	538	0.23	10
Slow brine injection	10	2.02×10^{-7}	7.68	18	10
Forced brine injection	700	1.54×10^{-5}	538	0.23	10

A custom X-ray transparent core holder was built using Delrin, nylon and epoxy resin materials (42). All fluid connections were made with low pressure liquid chromatography fittings. A Silurian dolomite rock from the Thornton formation, USA, was used as the porous medium. This rock is a sucrosic dolomite comprising more than 99% dolomite with a range of pore sizes from millimetre scale pores to pores of less than 1 µm (Fig. SI1). Fig. SI1 shows backscattered SEM images of a polished thin section of Silurian dolomite at three different magnifications and demonstrates the multiple-scale porosity of this rock.

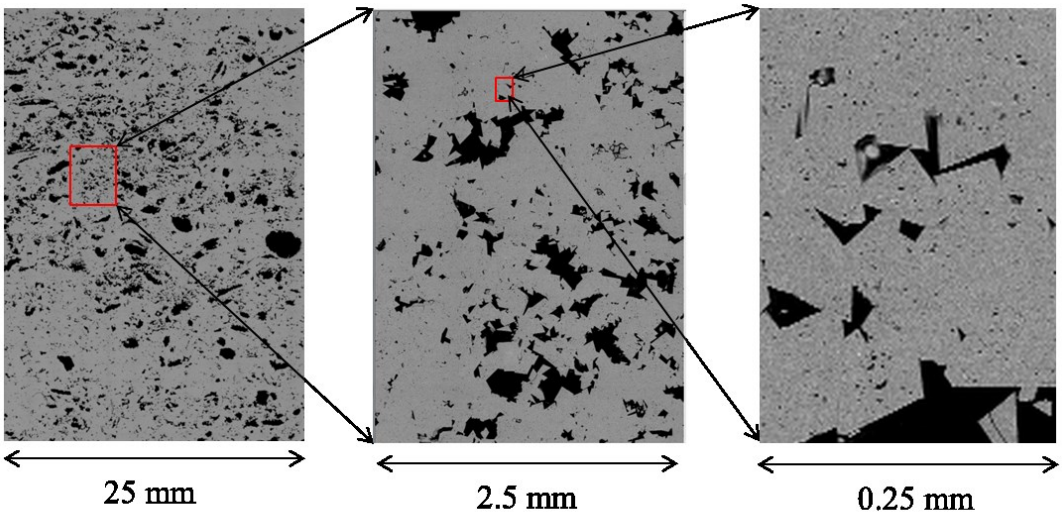

Figure SI1: Backscattered electron SEM image of a polished thin section of Silurian dolomite in three different magnifications, the carbonate rock display porosity over a range of pore sizes from sub-µm to mm scale.

Fig. SI2 shows mercury injection capillary pressure (MICP) results for three 25 mm diameter plugs of Silurian Dolomite. The MICP curves indicate that the rock has a well-connected pore network where 98% of the pore space of the rock is invaded at pressures less than 700 kPa. The pore throat distributions show three peaks at a radius of 16, 16, 14 µm for the three SD1, 2, 3 samples, respectively.

On average, 31% of the pore space of these plugs is connected to pore-throats that are below image resolution. Image resolution is 11.25 µm.

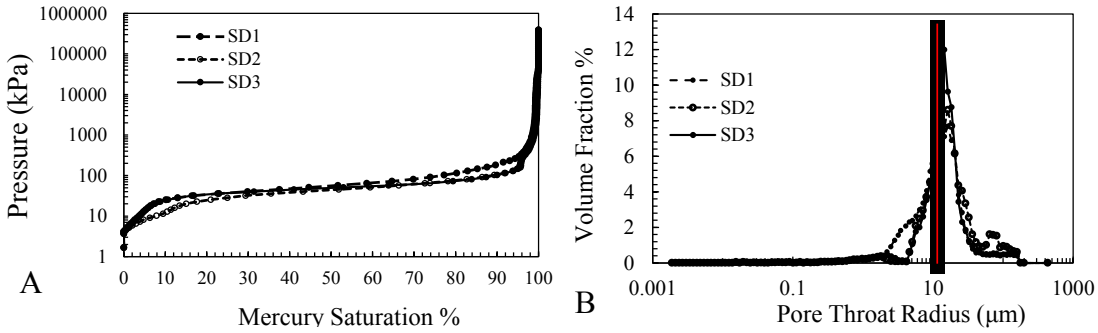

Figure SI2: Mercury injection capillary pressure test results for 3 Silurian dolomite plugs (2.54 cm diameter) showing (A) the capillary pressure-saturation curve and (B) the pore throat size distribution. The red line shows the limiting resolution of 11.25 µm for X-ray µCT imaging in this study. The volume fraction of pores connected to throats smaller than image resolution varies between 26 and 42 % with an average of approximately 31% for these three Silurian Dolomite core plugs.

Droplet Fragmentation

Fig. SI3 shows examples of fragmented oil droplets trapped in pores after the fast brine injection step at a scale of a few millimetres. All fragmented droplets are in contact with the pore walls when visualised in 3D

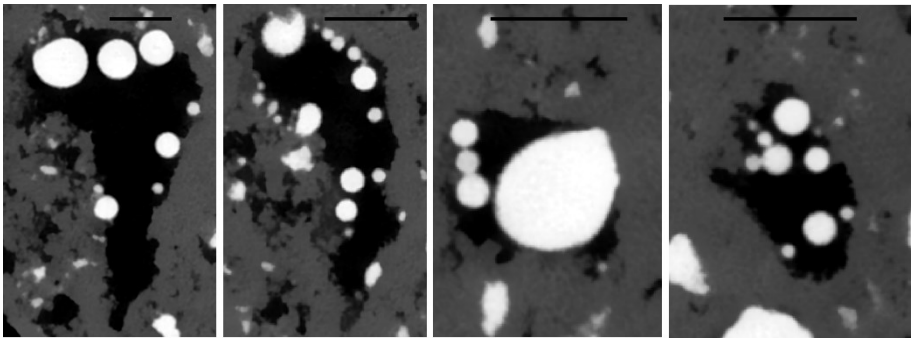

Figure SI3: 2D examples of fragmented oil droplets (white) in pores that are a few millimetres in size. The scale bar is 1 mm. The black colour represents the brine phase. Droplets that appear to be in free suspension are in contact with the pore surface when viewed in 3D.

Figs. SI4 and SI5 present two examples of fragmentation that occurred in pores with volumes of 10^{10} and 10^{8} µm^3, respectively.

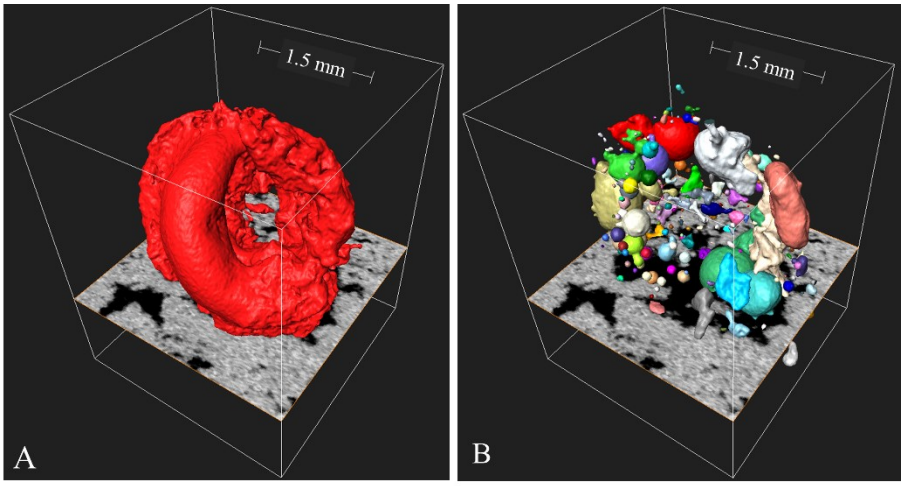

Figure SI4: 3D rendering of oil clusters after (A) slow (10 µl min^{-1}) and (B) fast (700 µl min^{-1}) brine injections. Pore volume of the order of 10^{10} μm^3 for (A) after slow brine injection and (B) oil after fast brine injection.

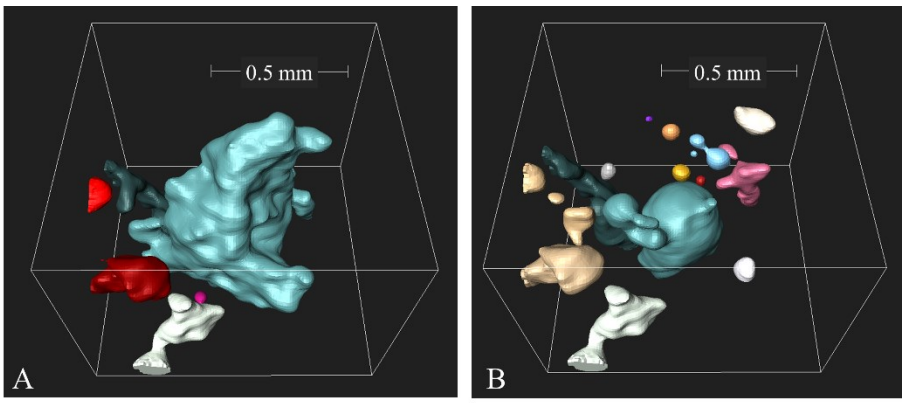

Figure SI5: 3D rendering of oil clusters for (A) slow (10 µl min^{-1}) and (B) fast (700 µl min^{-1}) brine injections. Pore volumes are on the order of 10^8 μm^3. This is an example of the smallest pores for which the droplet fragmentation mechanism can be observed.

Calculation of the fragmentation energies requires segmentation of the co-existing phases. The brine film is of sufficient thickness so that it can be segmented and visualised after fast imbibition. However, visual inspection of the data captured after slow imbibition suggests that the thickness of the brine film is different in different pores due to differences in capillary pressure acting in differently sized pores. Therefore, the segmentation of the brine film from these images remains uncertain. For the cases where snap-off has trapped an oil droplet in a single pore, the brine film appears to be thicker and hence can be segmented more easily (e.g. Fig.3). The brine film is thinner and more difficult to segment if the oil cluster spans a number of neighbouring pores (Figs. SI4 and SI5).

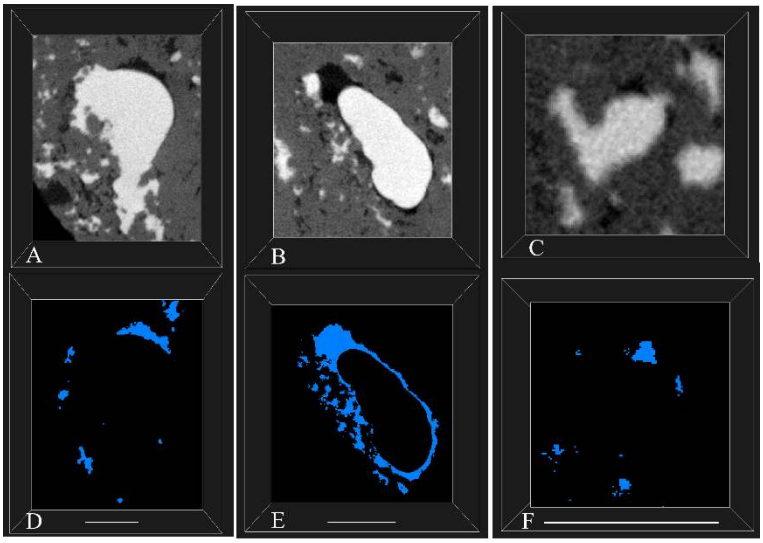

Figure SI6: Uncertainty in segmentation of the brine phase in the three pores presented in Figs. 3, SI4 and SI5, (A-C) greyscale µCT slices, (D-F) corresponding segmented brine phase. The brine phase is only well-segmented in the pore presented in (B,E). In the other two pores the brine phase is only partially segmentable. This causes an underestimation of the total surface energy. The scale bar is 1 mm.

If segmentation of brine film is not possible, the oil phase appears to be in direct contact with the rock surface, leading to an overestimation of the fraction of oil-solid contact area *f* and therefore to an underestimation of the total surface energy. For this reason, the calculated fragmentation energy (presented in Table SI2) is over-estimated for the two pores in Figs. SI4 and SI5.

Table SI2: Statistical analysis of the trapped oil phase for the pore presented in Figs. SI4 and SI5, respectively. Note that these are only exemplary for a number of droplet fragmentation events imaged in different pores.

	Pore volume μm^3	Brine injection $\mu l\ min^{-1}$	Number of oil droplets	Oil Volume μm^3	Oil-Brine Interface / Oil Volume μm^{-1}	Oil-Rock Contact/Oil Volume μm^{-1}	ΔE/Oil Volume	*f*
Pore in Fig. SI4	1.1×10^{10}	10	1	9.99×10^{9}	2.17×10^{-4}	7.28×10^{-3}	4.8	0.97
		700	242	2.95×10^{9}	5.03×10^{-3}	1.09×10^{-2}		0.68
Pore in Fig. SI5	2.01×10^{8}	10	5	1.88×10^{8}	7.09×10^{-4}	1.87×10^{-2}	2.32	0.96
		700	23	9.03×10^{7}	8.45×10^{-3}	2.15×10^{-2}		0.72

Fig. SI6 provides a measure of spheriodicity of the trapped oil droplets in the three pores depcited in Figs. 3, SI4 and SI5 by comparing their shape factor (surface area/ volume) with that of equivalent spheres (3/equivalent radius). The larger droplets have shapes that deviate from perfect

spheres due to the geometry of the pores confining them. For the smallest pore with a volume of 10^8 μm^3, the deviations stem from resolution limitations.

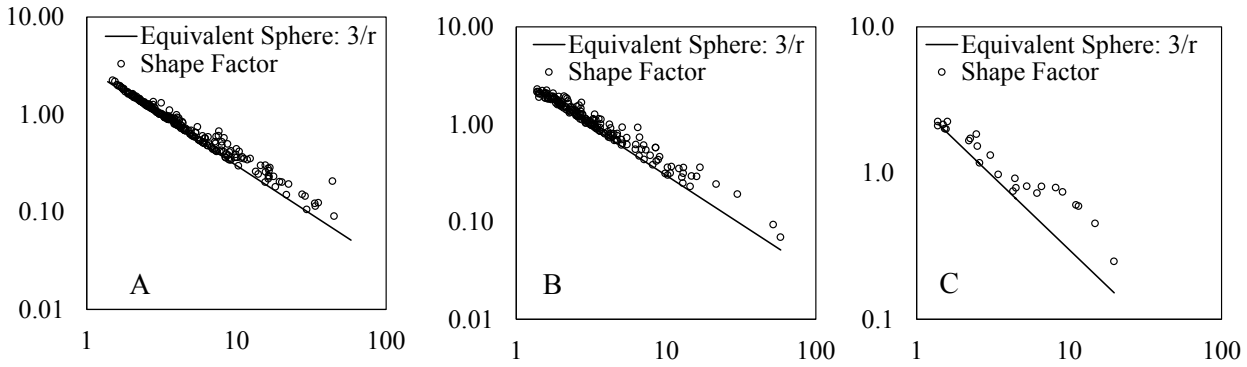

Figure SI7. Comparison of the sphericity expressed in terms of the shape factor (surface area/ volume) of the fragmented oil droplets for the pores presented in Figs. 3 (A), SI4 (B), and SI5 (C), respectively, with the shape factors for spheres (3/radius). Note that most fragmented droplets have shapes that are close to spherical.

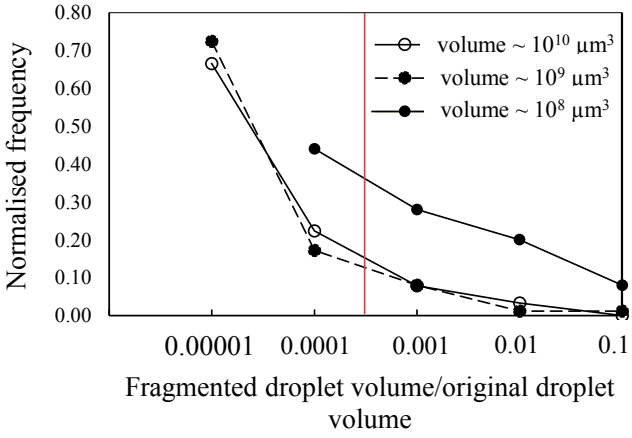

Figure SI8: Comparison between the volume of fragmented oil droplets and the volume of oil droplet trapped in the pore before fragmentation for the pores presented in in Figs. 3 (Pore 1), SI4 (Pore 2), and SI5 (Pore 3). 89 %, 90%, and 44 %, respectively, of the droplets are smaller than the volume of the original oil droplet by at least two orders of magnitude.

References:

1. Pak T, *et al.* (2013) Pore-Scale Visualisation of Two-Phase Fluid Displacement Processes in a Carbonate Rock using X-ray micro-Tomography Technique. in *SPE Reservoir Characterization and Simulation Conference and Exhibition* (Society of Petroleum Engineers, Abu Dhabi, UAE).